SIAM J. APPL. MATH.
Vol. 63, No. 2, pp. 538–563

A THERMOMECHANICAL MODEL FOR ENERGETIC MATERIALS WITH PHASE TRANSFORMATIONS: ANALYSIS OF SIMPLE MOTIONS*

JACK JAI-ICK YOH†, D. SCOTT STEWART†, AND GREGORY A. RUDERMAN‡

Abstract. This paper examines the behavior of a thermomechanical model for energetic materials posed in the companion paper and specifically analyzes three simple motions: (i) constant volume evolution, (ii) one-dimensional, time-dependent longitudinal compression (expansion), and (iii) time-dependent shear. The model describes phase transitions from solid to liquid to gas and exothermic chemical reaction. Thermal and mechanical properties are matched to the explosive HMX in order to illustrate representative dynamics and transitions. Constant volume thermal explosion, shock melting, and shear localization are demonstrated.

Key words. combustion, phase transformations, energetic materials

AMS subject classifications. 74A50, 74F10, 74F25, 74A15, 80A22, 80A25

PII. S003613990139026X

1. Introduction.

This paper (paper II) is the second of two papers that describe a continuum model for the behavior of a condensed phase energetic material that undergoes phase transformation. Such materials are often used in explosive and pyrotechnic systems and are commonly known as solid explosives. Explosive materials are usually stable solids at room temperature and pressure, and when subjected to sufficiently strong mechanical or thermal stimulus, they undergo transitions to liquid and gas before releasing the bulk of their stored energy by chemical reaction mainly in the gas phase. Paper I [2] presented the continuum formulation that describes phase transitions from solid to liquid to gas. The model also includes energy-release due to chemical reaction. The state of the phase and the progress of the chemical reaction are represented by two thermodynamically independent variables, ϕ and λ. The phase variable ϕ takes on the value 0 for a pure solid, 1 for a pure liquid, and 2 for a pure gas. The progress of the (exothermic) chemical reaction is represented by λ, which ranges from 0 (unreacted) to 1 (completely reacted).

Most of paper I explains the model's formulation and assumptions and the restricted form of the constitutive theory based on standard arguments from the second law of thermodynamics. Following Gurtin's suggestion [1], configurational forces are assumed to be in global and local balance and further arguments lead to the derivation of an evolution law for ϕ, which is of the advection, diffusion, reaction type. Following combustion theory for a reactive mixture, an evolution law for the reaction progress variable λ is posited as a fundamental law.

Hence, our model is fully three-dimensional and is thermodynamically and tensorially consistent. Specialization of the model and limiting forms are examined in

*Received by the editors June 4, 2001; accepted for publication (in revised form) April 29, 2002; published electronically November 19, 2002. This work was supported by the U.S. Air Force. This work was carried out with resources from the U.S. Air Force Research Laboratory, Armament Directorate, Eglin AFB, Florida, F08630-95-004, F08630-00-1-0002 and the U.S. Air Force Office of Scientific Research, Physical Mathematics Directorate, F49620-96-1-0260.

http://www.siam.org/journals/siap/63-2/39026.html

†Department of Theoretical and Applied Mechanics, University of Illinois, Urbana-Champaign, Urbana IL 61801 (yoh1@llnl.gov, dss@uiuc.edu).

‡Air Force Research Laboratory, Edwards Air Force Base, Edwards AFB, CA 93542 (Gregory.Ruderman@edwards.af.mil).

paper I, and the equations for the special cases of constant volume evolution, one-dimensional, time-dependent longitudinal compression motion and time-dependent shear motion are obtained. Solutions to initial boundary-value problems for the equations for these simple motions illustrate the behavior of the model and reveal its properties. The results testify to the model's potential suitability for modeling complex phenomena that involve both phase transformation and chemical reaction in one combined framework. Material constants and properties of the energetic material (solid explosive) HMX are used to determine representative values for the model. These include properties such as (but not limited to) the elastic properties, viscosities, specific heats, gas constant, heats of melting (fusion), vaporization (condensation), and combustion (detonation).

In section 2 the equations for the three-dimensional model are given. In section 3 we discuss how we assigned the material properties of HMX to the model. In section 4 the special forms of the equations for the three simple motions are indicated (and the reader is referred to paper I). We also solve the case for constant volume evolution and discuss the properties of the underlying ODEs and their dynamics. To avoid unnecessary repetition of previously stated equations, we will refer to the equations as follows. For (6.1) of paper I, we will write (I 6.1). In section 5 the numerical methodology is given for longitudinal and shear motions. Section 6 presents representative numerical solutions for mechanically induced phase transformation and includes examples of interesting properties of the model such as shear localization and shock melting.

2. Mathematical formulations.

2.1. Kinematics and some definitions. The coordinates of position in the lab-frame are given by $\boldsymbol{x}$ and the initial position of the material particles is given by $\boldsymbol{X}$. The mapping of the deformations is given by $\boldsymbol{x} = \boldsymbol{x}(\boldsymbol{X}, t)$. The deformation gradient $\boldsymbol{F}$ is defined by the derivative $\boldsymbol{F} = \partial\boldsymbol{x}/\partial\boldsymbol{X}$. The left Cauchy–Green tensor $\boldsymbol{B} = \boldsymbol{F}\boldsymbol{F}^T$ is used to describe finite deformations. The velocity is defined by the time derivative of the particle trajectories $\boldsymbol{v} = (\partial\boldsymbol{x}/\partial t)_{\boldsymbol{X}}$. The velocity gradient is the gradient of the velocity field defined by the tensor $\boldsymbol{L} = \vec{\nabla}\boldsymbol{v}$. Let the dot notation, $\dot{(\,)}$, refer to the material derivative. The rate of stretching tensor is given by $\boldsymbol{D} = [\vec{\nabla}\boldsymbol{v} + (\vec{\nabla}\boldsymbol{v})^\top]/2$. The time derivative of the deformation gradient is $\dot{\boldsymbol{F}} = \boldsymbol{L}\boldsymbol{F}$. Consideration of conservation of mass relates the instantaneous density ρ to a reference (ambient) density of the solid, ρ_0, by $\det(\boldsymbol{F}) = \rho_0/\rho$ as well as $\det(\boldsymbol{B}) = (\rho_0/\rho)^2$.

2.2. General formulation. The derivation of the model and its constitutive specification was the principal subject of paper I [2]. The arguments in paper I developed a ϕ-dependent constitutive expression for the stress $\boldsymbol{\sigma}$ as

$$\begin{aligned}\boldsymbol{\sigma} = {} & \mu_s \frac{\rho}{\rho_0}\boldsymbol{B} - \mu_c \frac{\rho}{\rho_0} III_{\mathbf{B}}^{-[\nu_c/(1-2\nu_c)]}\boldsymbol{I} + \mu_l \frac{\rho}{\rho_0} III_{\mathbf{B}}^{1/3}\boldsymbol{I} \\ & - \alpha_c K \frac{\rho}{\rho_0}(T - T_0)\boldsymbol{I} - \rho R_g T \boldsymbol{I} \\ & - \rho\gamma_\phi \vec{\nabla}\phi \otimes \vec{\nabla}\phi + \nu_f(\vec{\nabla}\cdot\boldsymbol{v})\boldsymbol{I} + 2\mu_f \boldsymbol{D}\,. \end{aligned} \tag{2.1}$$

The material properties μ_c, μ_s, μ_l, α_c, R_g, γ_ϕ, ν_f, and μ_f are assumed to be functions of ϕ such that they are nonzero in the appropriate phase and are zero otherwise. The shear modulus μ_s is associated with a Blatz–Ko compressible solid and μ_l is associated with a liquid. The function μ_c represents the shear modulus of the condensed phase

such that $\mu_c = \mu_s + \mu_l$, with the properties that $\mu_c(0) = \mu_s(0) = \mu_{solid}$, $\mu_l(0) = 0$, $\mu_s(1) = 0$, $\mu_c(1) = \mu_l(1) = \mu_{liquid}$, and $\mu_c(2) = \mu_s(2) = \mu_l(2) = 0$. The function α_c is associated with a thermal expansion stress, R_g is associated with the ideal gas constant in a gas, ν_f and μ_f are associated with strain rate generated viscous stress, and γ_ϕ is associated with phase change induced stresses that act in regions with nonzero phase gradients. Derivatives of the ϕ-dependent functions appear as $\alpha'(\phi, T) = \partial\alpha/\partial\phi|_T$. The "$s$" subscript refers to the solid phase, the "l" subscript refers to the liquid phase, and the "c" subscript refers to the condensed phase. Similarly the "f" subscript refers to the fluid properties for both liquid and gas phases. If spelled out, the subscript "solid," "liquid," or "gas" refer to a constant material property. The various scalar material properties, such as c_v, γ_ϕ, could have explicit dependence on λ as well as ϕ and T. The governing equations for the model with reaction and phase change (without body forces) are

$$\dot{\rho} + \rho\vec{\nabla}\cdot\boldsymbol{v} = 0\,, \tag{2.2}$$

$$\rho\,\dot{\boldsymbol{v}} = \vec{\nabla}\cdot\boldsymbol{\sigma}\,, \tag{2.3}$$

$$\begin{aligned}
\rho c_v\dot{T} &= \vec{\nabla}\cdot(k\vec{\nabla}T) + \nu_f(\vec{\nabla}\cdot\boldsymbol{v})^2 + 2\mu_f\boldsymbol{D}:\boldsymbol{D} + B\dot{\phi}^2 \\
&\quad - \alpha_c K\frac{\rho}{\rho_0}T(\vec{\nabla}\cdot\boldsymbol{v}) - \rho R_g T(\vec{\nabla}\cdot\boldsymbol{v}) \\
&\quad + \left\{-\frac{\alpha_c'(\phi)}{2}K\frac{\rho}{\rho_0}T\ln(III_{\mathbf{B}}) - \rho\frac{R_g'(\phi)}{2}T\ln(III_{\mathbf{B}}) - \rho c_v'(\phi)T\ln(T/T_0)\right. \\
&\quad \left. + \rho\left[\beta_m'(\phi)\frac{T}{T_m}Q_m + \beta_v'(\phi)\frac{T}{T_v}Q_v\right]\right\}\dot{\phi} + \rho Q_{hc}\,\Omega + \rho r\,,
\end{aligned} \tag{2.4}$$

$$\begin{aligned}
B\dot{\phi} &= \vec{\nabla}\cdot\left(\rho\gamma_\phi\vec{\nabla}\phi\right) + \rho c_v'(\phi)\left[T\ln(T/T_0) - (T - T_0)\right] \\
&\quad - \frac{\mu_s'(\phi)}{2}\frac{\rho}{\rho_0}(I_{\mathbf{B}} - 3) - \frac{\mu_c'(\phi)}{2}\frac{\rho}{\rho_0}\frac{(1-2\nu_c)}{\nu_c}\left(III_{\mathbf{B}}^{-\nu_c/(1-2\nu_c)} - 1\right) \\
&\quad + \frac{3\mu_l'(\phi)}{2}\frac{\rho}{\rho_0}III_{\mathbf{B}}^{1/3} \\
&\quad + \frac{\alpha_c'(\phi)}{2}K\frac{\rho}{\rho_0}(T - T_0)\ln(III_{\mathbf{B}}) + \frac{1}{2}\rho R_g'(\phi)T\ln(III_{\mathbf{B}}) \\
&\quad - \rho\frac{1}{2}\Psi^{well}\frac{\partial F}{\partial\phi} - \rho\left[\beta_m'(\phi)\left(\frac{T}{T_m} - 1\right)Q_m + \beta_v'(\phi)\left(\frac{T}{T_v} - 1\right)Q_v\right],
\end{aligned} \tag{2.5}$$

$$\rho\dot{\lambda} = \vec{\nabla}\cdot(d\vec{\nabla}\lambda) + \rho\,\Omega\,, \tag{2.6}$$

$$\dot{\boldsymbol{F}} = \boldsymbol{L}\boldsymbol{F}\,. \tag{2.7}$$

Table 1 gives the values for material properties that appear in (2.1)–(2.7). The values are based upon HMX along with references to the data source or a notation that we have used a model value.

2.3. Material transition functions. An important ingredient of our model is the use of ϕ-dependent material properties, or material transition functions. Their most prominent use is in the definition of the source terms in the ϕ-evolution equation and the energy (temperature) equation. Also, functions such as $\mu_c(\phi)$, $\mu_s(\phi)$, $\mu_l(\phi)$, $\alpha_c(\phi)$, $R_g(\phi)$, $c_v(\phi)$ all change with the phase variable ϕ. The model assumes that these are defined in such a way so that they take on proper values for pure phases when the material has the limiting pure-phase values for ϕ. The ϕ-dependent material

TABLE 1
Material properties typical of HMX.

Material property	Value	Refs.
density of β-HMX (ρ_0)	1.71 g/cm^3	[7]
density of liquid-HMX	1.65 g/cm^3	[13]
specific heat at constant volume (c_v)	1.5×10^3 J/kg K	[7]
isothermal bulk modulus ($K = \rho \left.\frac{\partial p}{\partial \rho}\right\|_T$)	13.5 GPa	[7]
shear modulus (μ_{solid})	2.46 GPa	modeled
shear modulus (μ_{liquid})	2.37 GPa	modeled
Poisson's ratio (ν_c)	0.414	calculated
viscosity coefficient (μ_f)	0.45 N s/m^2	[5]
bulk viscosity coefficient (ν_f)	-2/3 μ_f	Stokes hypothesis
thermal expansion coefficient (α_{solid})	0.000134 1/K	[7]
thermal conductivity (k)	.36 W/m K	[7]
phase diffusion coefficient ($\rho\gamma_\phi$)	1.0×10^{-6} m kg/s^2	modeled
universal gas constant (R_u)	8313 J/kmole K	
molar weight of β-HMX	296.2 kg/kmole	[5]
gas constant per unit mass (R_{gas})	300 J/kg K	modeled
melting temperature (T_m)	558 K	[5]
vaporization temperature (T_v)	588 K	modeled
heat of melting (Q_m)	-200×10^3 J/kg	[5]
heat of vaporization (Q_v)	-100×10^3 J/kg	modeled
heat of combustion (Q_{hc})	5.0×10^6 J/kg	[8]
rate of heat source (ρr)	5000 J/m^{3}s	modeled
frequency of Arrhenius kinetic (A)	9.3×10^{16} 1/s	[8]
activation temperature (E_a/R_u)	24660 K	[8]
depth of phase well (Ψ^{well})	550 J/kg	modeled
multiplication factor of $\dot{\phi}$ (B)	1.5 kg/m s	modeled

transition functions used for this paper are listed in the appendix and are made up of simple, smooth, or piece-wise smooth polynomials in ϕ.

Figure 1 shows the material transition functions $\beta'_m(\phi)$, $\beta'_v(\phi)$ that are used to construct ψ_2, which represents free-energy changes during phase transition and is given by

$$\psi_2 = \frac{1}{2}\Psi^{well}F(\phi) + \beta_m(\phi)Q_m\Big(\frac{T}{T_m} - 1\Big) + \beta_v(\phi)Q_v\Big(\frac{T}{T_v} - 1\Big), \tag{2.8}$$

where $\Psi^{well} > 0$ is a constant that describes the potential and $Q_m < 0$ and $Q_v < 0$ are constants representing the heats of melting and vaporization. The constants $T_m > 0$ and $T_v > 0$ are melting and vaporization temperatures. Here we assume a specific form for $F(\phi)$ (listed in the appendix) that is a smooth positive definite function with isolated zeros at $\phi = 0, 1$, and 2 representing three local minima. In addition, $F(\phi)$ is assumed to be locally quadratic near the zeros at $\phi = 0, 1$ and 2, i.e., near $\phi = 0$, $F \sim \phi^2$, near $\phi = 1$, $F \sim (\phi - 1)^2$, and near $\phi = 2$, $F \sim (\phi - 2)^2$. The function $\beta_m(\phi)$ is assumed to be smooth and monotonically increasing and has values from 0 to 1 on the range $0 \le \phi \le 1$ with zero derivative elsewhere. Similarly, the function $\beta_v(\phi)$ is assumed to be monotonically increasing with values from 0 to 1 on the range $1 \le \phi \le 2$. The derivative of transition energy density $\partial\psi_2/\partial\phi$ generates source terms

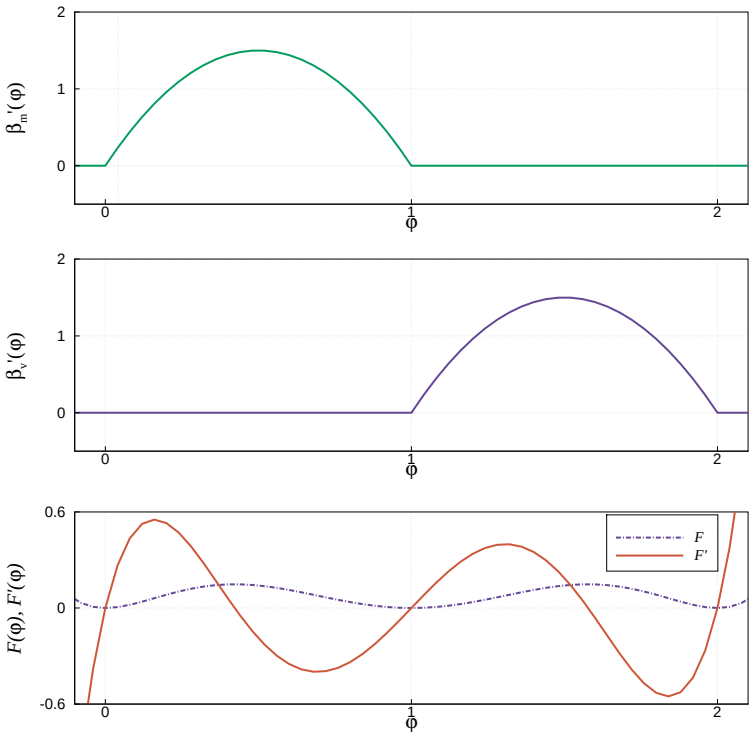

FIG. 1. *Material transition functions β_m' and β_v' and Ginzburg–Landau potential F used to prescribe the phase transition energy density ψ_2.*

in the phase equation represented as

$$\frac{\partial \psi_2}{\partial \phi} = \frac{1}{2}\Psi^{well}\frac{\partial F}{\partial \phi}(\phi) + \beta_m'(\phi)Q_m\Big(\frac{T}{T_m} - 1\Big) + \beta_v'(\phi)Q_v\Big(\frac{T}{T_v} - 1\Big). \tag{2.9}$$

Figure 2 illustrates the assumed dependence of $\psi_2(\phi, T)$ on ϕ and T. Starting from (a) through (d), the temperature T is raised from below T_m to above T_v, representing a standard melting-evaporation process. The transition energy density in (a) has its minimum at $\phi = 0$. As T is increased through T_m and then T_v, we see a shift in the global minima from pure solid to solid-liquid and to liquid-vapor. As T eventually exceeds T_v as shown in (d), the energy minimizing well shifts to a vapor state at $\phi = 2$. Figure 3 shows examples of the other material transition functions and their derivatives.

3. Matching material properties to HMX. Here we discuss our fit of the model's material properties to mimic an energetic material like HMX. Figure 4 shows a pressure-temperature plane that indicates regions where, from classical and experimental considerations, HMX can be considered to be a static solid, liquid, or a gas in thermodynamic equilibrium. Some of the boundaries (specifically the solid/liquid boundary) are known from experiment. Note that solid phases of HMX are not differentiated here, and it is assumed that the β-phase of solid HMX is representative. The solid/liquid boundary is of particular interest and is computed via a Kraut–Kennedy law. It is well known that HMX liquid is quite unstable [3] and once the liquid phase

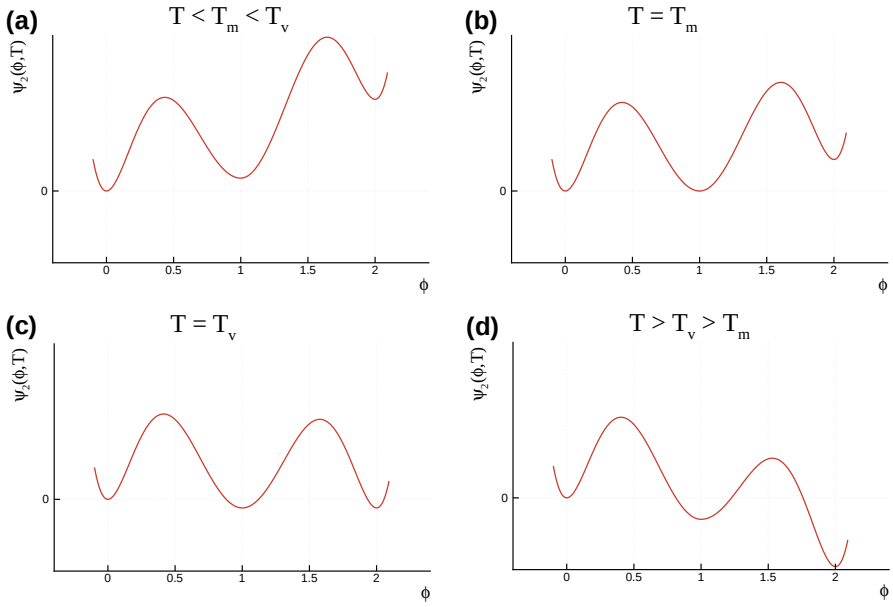

FIG. 2. *Plot of ψ_2 as a function of ϕ with T variation.*

appears it quickly evolves into gas, partly from exothermic energy released by chemical reaction in the condensed phase. For the purpose of our early modeling efforts, we have decided to match the HMX melt temperature to the experimental melt temperature $T = 558$ K and the evaporation temperature at $T = 588$ K. Figure 4 shows a shaded box that represents the range of temperatures and pressures (level of stress) predicted by computation with model.

In our model, p-V isotherms (where $V = 1/\rho$) can be obtained directly from (2.1) by setting all derivatives equal to zero and by assuming a homogeneous deformation such that $\boldsymbol{B} = (\rho_0/\rho)^{2/3}\boldsymbol{I}$ and $\boldsymbol{\sigma} = -p\boldsymbol{I}$ (where p is the pressure) to obtain

$$p = \mu_c \left(\frac{\rho}{\rho_0}\right)\left[\left(\frac{\rho}{\rho_0}\right)^{\frac{2\nu_c}{1-2\nu_c}} - \left(\frac{\rho}{\rho_0}\right)^{-\frac{2}{3}}\right] + \alpha_c K \frac{\rho}{\rho_0}(T - T_0) - \rho R_g T\,. \tag{3.1}$$

HMX liquid is approximately 4% less dense than HMX solid [13]. Figure 5 shows a plot of an isotherm computed from (3.1) with values shown in Table 1. Experimental data points on the solid isotherms obtained by Yoo and Cynn [10] are shown for comparison. Since HMX liquid is so chemically unstable, experimental data for the liquid isotherm is not available. One implication of the lower density for HMX liquid is that the isothermal sound speed (the negative slope of the p-V isotherm) is greater in the solid than in the liquid. Figure 6 shows a plot of an isotherm computed from (3.1) for the ideal gas term that is proportional to R_g. Figure 7 shows a representative isotherm on log-scales at 300 K, for the full range of values for the model when the material is solid, liquid, or gas, as computed from (3.1).

4. Form of the model for three simple motions. Here we consider the differential equations for the model when the material undergoes three simple motions: (i) evolution at constant volume, (ii) time-dependent longitudinal motion, and (iii)

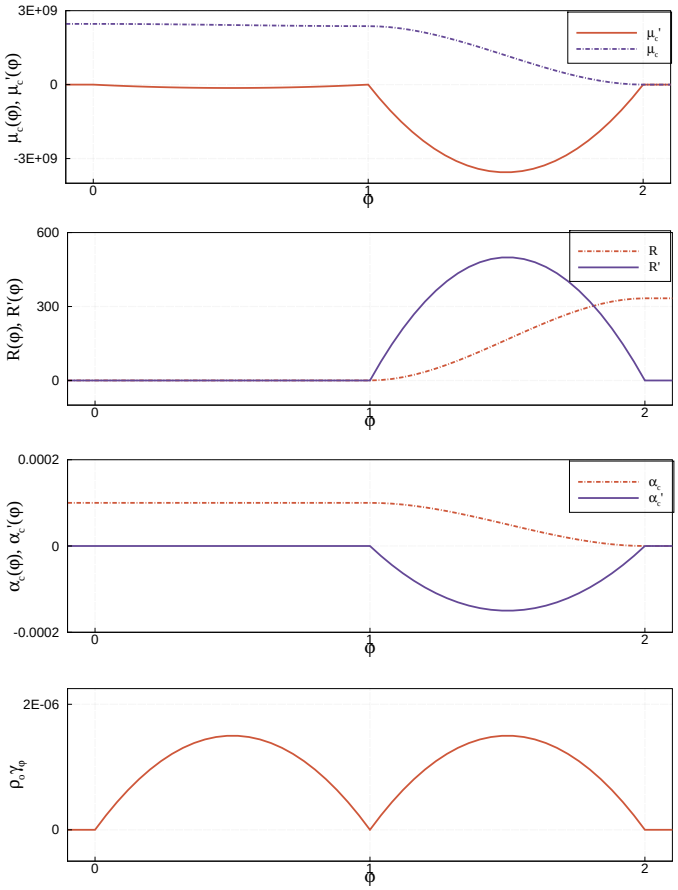

FIG. 3. *Plots of transition functions and their derivatives for the HMX simulant derivatives with respect to the phase variable. Shear modulus, ideal gas constant, thermal expansion coefficient, and phase diffusion coefficient are shown from top to bottom.*

one-dimensional, time-dependent shear motion. All three cases are amenable to extensive computational and theoretical analysis and their discussion reveals the underlying mathematical properties of the model. All three are very important in the traditional analysis of ignition of energetic materials. The reduction for the three special motions follow directly from the general form of equations (2.1)–(2.7) and were derived in the last section of paper I.

4.1. Evolution at constant volume. An important simple case often considered in combustion theory describes constant volume thermal explosion, where the velocity $\boldsymbol{v}$ as well as all spatial gradients are exactly zero and the density is constant. For illustration (in this section only), we neglect thermal expansion and assume a constant specific heat and gas constant. We are left with three ODEs in time for the temperature T, phase variable ϕ, and reaction progress variable λ (see (I 6.1), (I 6.2), and (I 6.3)). If phase change is discarded, we recover the equations from standard combustion theory for constant volume thermal explosion, $c_v(\partial T/\partial t) = Q_{hc}\,\Omega\,, (\partial\lambda/\partial t) = \Omega$. Of course, the more interesting behavior occurs when phase change is included.

Figure 8 shows an example of the time evolution of constant volume heating

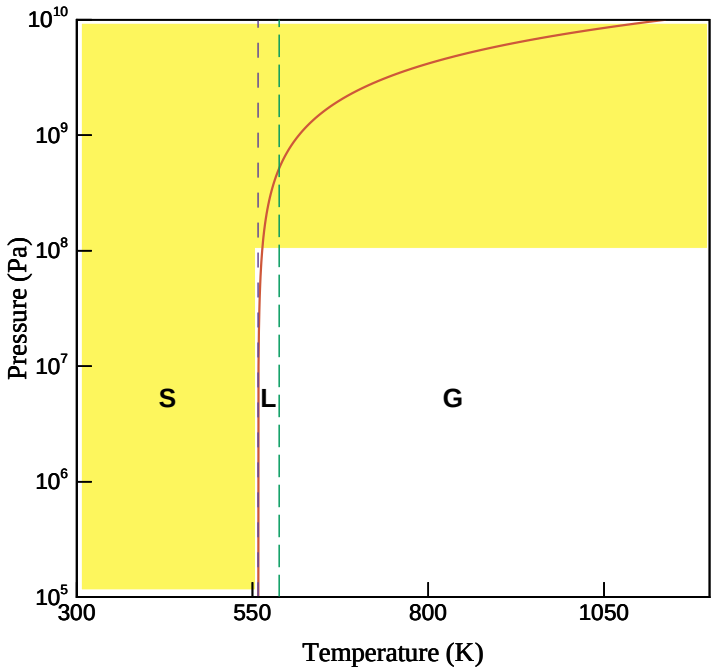

FIG. 4. *The solid curve is the melt temperature-pressure relation for β-HMX given by the semi-empirical Kraut–Kennedy law* [4], [7]. *Dashed line and long-dashed line are constant melt temperature and vapor temperature used in the current numerical simulation, respectively.*

without chemical reaction starting from a solid ($\phi = 0$) at an initial temperature of $T = 300$ K. The heating rate r and the kinetic parameter B control the transformation rates. It is possible to see (at least qualitatively) all of the phase change behaviors expected during constant volume heating. As heat is first applied, the temperature increases linearly. As the temperature increases further, the material begins to melt and the endothermic process absorbs heat from the system. (In Figure 8 the slight temperature decrease is barely visible in the nearly constant temperature interval.) At the completion of the phase transformation to liquid, the temperature rises in the liquid at a constant rate until the vaporization temperature is reached and second phase transition from liquid to gas phase occurs. After that, constant rate heating in the gas occurs.

The sharp transitions that are apparent in Figure 8 (for example, near the times $t = 0.05$ and $t = 0.09$ sec) are the result of a bifurcation and a change of stability in the ODEs near the transition temperatures T_m and T_v. To see this clearly, consider the stability of the solid phase during constant rate heating. The temperature and the phase variable can be represented to leading order as $T = T_0 + r\,t/c_v$ and $\phi = 0$ (with $\lambda = 0$ for all time), so that a stability analysis assumes that T and ϕ take the form

$$T = T_0 + \frac{r}{c_v}t + T'(t) + \cdots, \qquad \phi = \phi'(t) + \cdots, \tag{4.1}$$

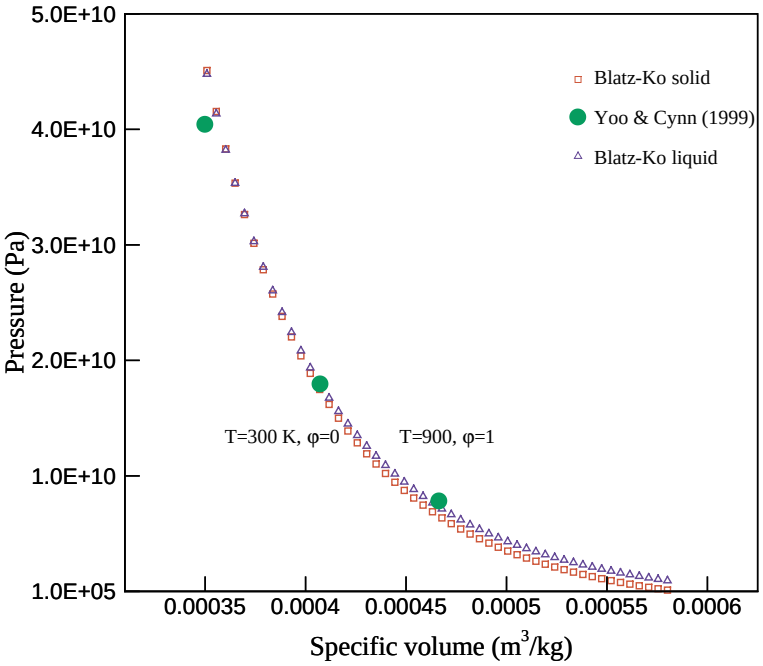

FIG. 5. *P-V isotherms at $T = 300\ K$ and $T = 900\ K$. $\left|\frac{dp}{dV}\right|_{\phi=0} > \left|\frac{dp}{dV}\right|_{\phi=1}$ implies that the speed of sound is greater in solid than in the liquid HMX.*

where T' and ϕ' are assumed to be small. The linearization of (I 6.1), (I 6.2) with $\beta'_m \approx 6\phi'$ and $\partial F/\partial\phi \approx 8\phi'$ is straightforward and leads to equations for T', ϕ':

$$\frac{dT'}{dt} = 0\,, \tag{4.2}$$

$$\frac{d\phi'}{dt} = -\frac{\rho}{B}\left\{4\Psi^{well} - 6Q_m\left(1 - \frac{T^{(0)}}{T_m}\right)\right\}\phi'\,, \tag{4.3}$$

where $T^{(0)}$ is the leading-order temperature found from simple constant rate heating

$$T^{(0)} = T_0 + \frac{r}{c_v}t\,. \tag{4.4}$$

The stability properties of the solution for ϕ' are governed by the sign of $d\phi'/dt$ found on the right-hand side of (4.3). For early times, the argument is always negative, since $T^{(0)} < T_m$ and $Q_m < 0$. Consequently, the solution is exponentially stable. (It is a simple matter to write down the exact solution of (4.3).) As the temperature rises, the stability changes as $d\phi'/dt$ changes sign, and this time it is found by setting the right-hand side of (4.3) exactly equal to zero. In this case the leading-order temperature is

$$T^{(0)} = T_m - \frac{2}{3}\frac{\Psi^{well}}{Q_m}T_m\,. \tag{4.5}$$

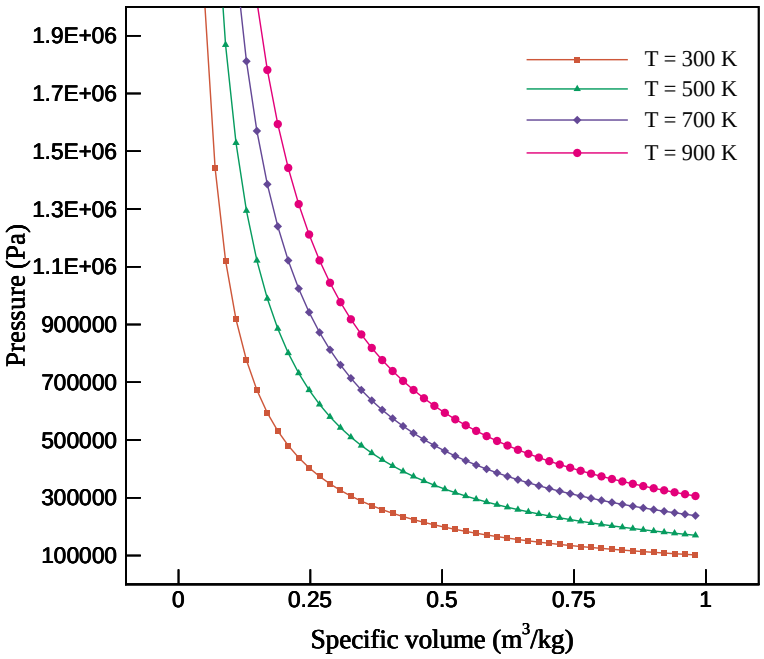

FIG. 6. *P-V isotherms at four different temperatures for HMX vapor ($\phi = 2$).*

For the case where $|\Psi^{well}/Q_m| << 1$, the phase transition temperature associated with this simple change of stability is close to T_m. So we find that below the melt temperature the perturbations are stable, but near the melt temperature the stability changes type and becomes unstable. Any perturbation grows and subsequently an abrupt transition occurs from $\phi = 0$. Another point is that our assumed properties for F strictly require a nonzero perturbation of ϕ to be combined with heating in order to observe a phase transition. In cases other than constant volume evolution, other source terms exist in the ϕ-evolution equation (specifically those related to derivatives of the Helmholtz free energy associated with deformation) and they can be the source of thermomechanical disturbances that can grow when the phase becomes dynamically unstable.

Figure 9 shows a representative solution to (I 6.1)–(I 6.3) with an Arrhenius form assumed for $\Omega = A(\phi)(1-\lambda)\exp[-E_a/(R_u T)]$. The function $A(\phi)$ is chosen to be zero in the solid phase and takes the value listed in Table 1 in the gas phase. Initially the material is solid and cold and heated at a uniform rate. So the phase transformations from solid to liquid to gas occur in the same way as shown in Figure 8. However, for this example, once the gas is in abundance, the chemical reaction starts and the gas undergoes a classically well understood constant volume thermal explosion. If we had chosen to adopt a more complex kinetic form for Ω, reaction could take place first in the liquid phase. In the near future, we plan to use more realistic kinetic scheme for HMX. Clearly there is the flexibility within this formulation to model many aspects of condensed phase energy release.

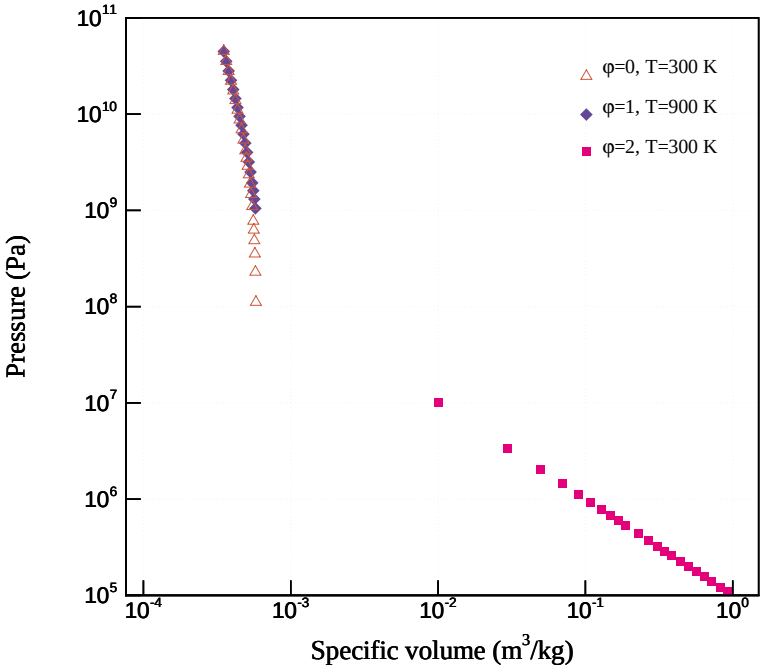

FIG. 7. *P-V isotherms for solid, liquid, and vapor HMX at $T = 300$ K, drawn to a single range of P-V axes.*

4.2. Longitudinal motion. Next we consider simple longitudinal motion. Typically, explosives are tested by subjecting them to impact with a flyer-plate. In an idealization of this experiment, an infinite slab experiences a displacement loading normal to its surface. As a computational matter, the same flow can be modeled as a reverse impact experiment, where the sample is set into uniform motion and suddenly comes to rest at the origin. We must consider following one-dimensional motion:

$$x_1 = X_1 + f_1(X_1, t)\,, \quad x_2 = X_2\,, \quad x_3 = X_3\,, \tag{4.6}$$

where f_1 is the displacement in the 1-direction. There is one nonzero velocity component, $v_1 = \partial f_1/\partial t|_{\boldsymbol{X}}(X_1, t)$, and $\boldsymbol{F}$ and $\boldsymbol{B}$ are both diagonal, and $B_{11} = (1 + f_1')^2$, $B_{22} = 1, B_{33} = 1$. The first and third invariants of $\boldsymbol{B}$ are $I_{\boldsymbol{B}} = 2 + (1 + f_1')^2$ and $III_{\boldsymbol{B}} = (1 + f_1')^2 = (\rho_0/\rho)^2$. Then $I_{\mathbf{B}} - 3 = (\rho_0/\rho)^2 - 1$. Hence we use the density as the independent strain measure and replace f_1'. The one nonzero component of the rate of strain tensor is $D_{11} = \partial v_1/\partial x_1$. Also $(\vec{\nabla}\phi \otimes \vec{\nabla}\phi)_{11} = (\partial\phi/\partial x_1)^2$. It follows that all the shear stresses are zero, $\sigma_{12} = \sigma_{23} = \sigma_{13} = 0$, and the normal stress σ_{11}, is given by (I 6.5).

The governing equations for longitudinal compression are the mass and momentum equations in (I 6.6), (I 6.7), the energy equation (written in temperature form) in (I 6.8), and the phase and reaction progress evolution equations, given by (I 6.9) and (I 6.10). This special formulation is a set of five PDEs for the dependent variables ρ, v_1, T, ϕ, and λ in terms of the independent variables x_1 and t.

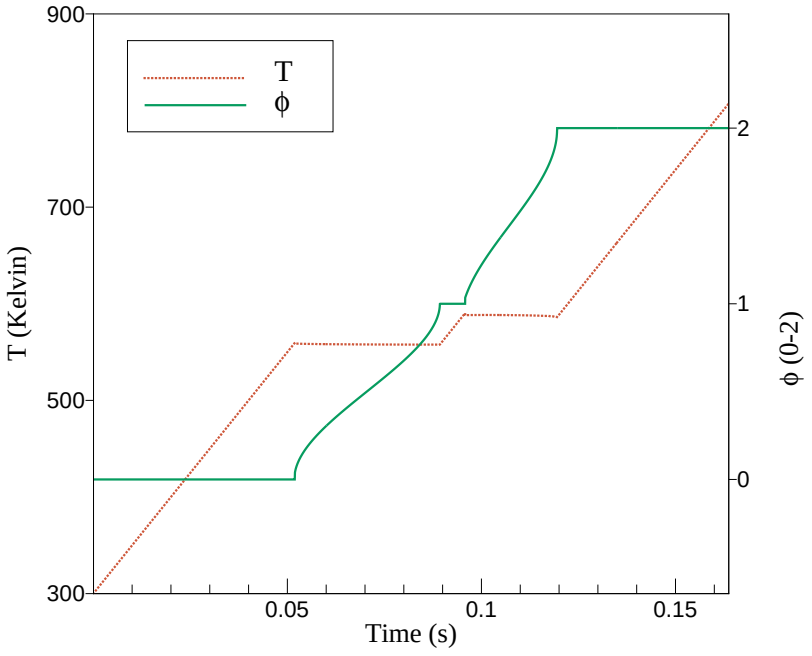

FIG. 8. *Constant volume phase transformation without reaction.*

4.3. Shear motion. The specialization of the equations to shear motion leads to PDEs in one space variable and time. The nominal geometry is a slab of fixed thickness loaded at one surface with constant velocity. The other surface is taken to be fixed (zero displacement) for the entire duration of the test. We consider the following shear motion:

$$x_1 = X_1 + f_1(X_2, t), \qquad x_2 = X_2 + f_2(X_2, t), \qquad x_3 = X_3\,, \tag{4.7}$$

where f_1 and f_2 are the in-plane displacements, which can also be regarded as functions of the spatial coordinate and time x_2, t. Corresponding to this motion one has the velocities with $v_1(x_2,t), v_2(x_2,t)$, $v_3 = 0$, and $\partial/\partial x_1 = \partial/\partial x_3 = 0$. The expression of the material time derivative is given by $\dot{\overline{()}} = \partial/\partial t + v_2\,\partial/\partial x_2$. The shear deformation is described by (I 6.12) and (I 6.13). The invariants of $\boldsymbol{B}$ are computed as $I_{\mathbf{B}} = 1 + {f_1'}^2 + (1+f_2')^2 + 1$ and $III_{\mathbf{B}} = (1+f_2')^2 = (\rho_0/\rho)^2$ with $1 + f_2' = \rho_0/\rho$. Also $I_{\mathbf{B}} - 3 = (\rho_0/\rho)^2 - 1 + {f_1'}^2$. In addition, from the kinematic identity $\dot{\boldsymbol{F}} = \boldsymbol{L}\boldsymbol{F}$, we obtain two nontrivial relations $\dot{f}_1' = (1+f_2')\partial v_1/\partial x_2$ and $\dot{f}_2' = (1+f_2')\partial v_2/\partial x_2$, where the material derivative is $\dot{\overline{()}} = \partial/\partial t + v_2\,\partial/\partial x_2$. The second of the two results is equivalent to replacing $1 + f_2'$ with ρ_0/ρ. The first is an independent expression for the shear strain which can be recast in terms of the density and transverse velocity gradient as in (I 6.14). Finally, $\vec{\nabla}\phi \otimes \vec{\nabla}\phi$ has only one nonzero component, $(\vec{\nabla}\phi \otimes \vec{\nabla}\phi)_{22} = (\partial\phi/\partial x_2)^2$.

We use the density ρ and the shear strain f_1' as the two independent kinematic

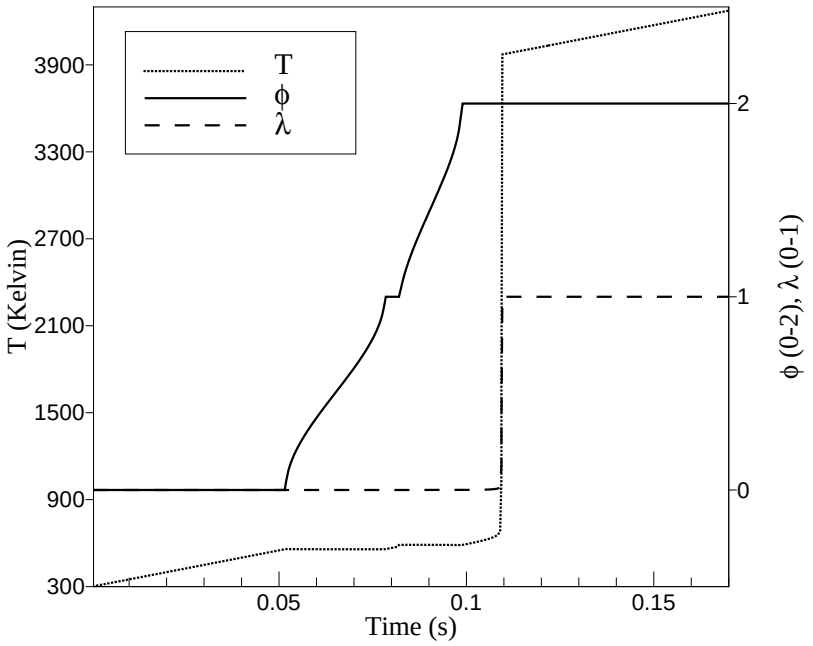

FIG. 9. *Constant volume thermal explosion.*

variables. We can now write down expressions for the components of the stress tensor. The cross-plane shear stresses are zero, i.e., $\sigma_{13} = \sigma_{23} = 0$. The in-plane shear stress σ_{12} is given by the expression (I 6.15). The in-plane normal stress σ_{22} is given by (I 6.16).

The specific governing equations for the shear motion are listed in (I 6.17)–(I 6.22). Finally the kinematic relation (I 6.14) for the shear strain (which must be included) is expressed as in (I 6.23). This special formulation is a set of seven PDEs for the dependent variables $\rho, v_1, v_2, T, \phi, \lambda$, and f_1' in terms of the independent variables x_2 and t.

5. Numerical methodology. We have implemented an efficient high-order temporal scheme for stiff equations based on the method of lines (MOL) to solve for longitudinal and shear motions. The MOL can be implemented for various choices of spatial discretization. For discretization of convective terms we use a fourth-order convex essentially nonoscillatory (ENO) method [6] combined with a third-order, low-storage, semi-implicit Runge–Kutta method [9] for the MOL-ODEs. We do not describe the ENO discretization here. Interested readers are referred to [6].

5.1. Description of low-storage semi-implicit Runge–Kutta solver. A more comprehensive discussion of the temporal scheme can be found in [9], and only a brief description of the method is given below. To solve a system of autonomous ODEs of the form $\boldsymbol{u}' = \boldsymbol{f}(\boldsymbol{u}) + \boldsymbol{g}(\boldsymbol{u})$, we use an explicit scheme for the nonstiff term $\boldsymbol{f}$ and an implicit scheme for the stiff term $\boldsymbol{g}$. We solve the system in an explicit/implicit

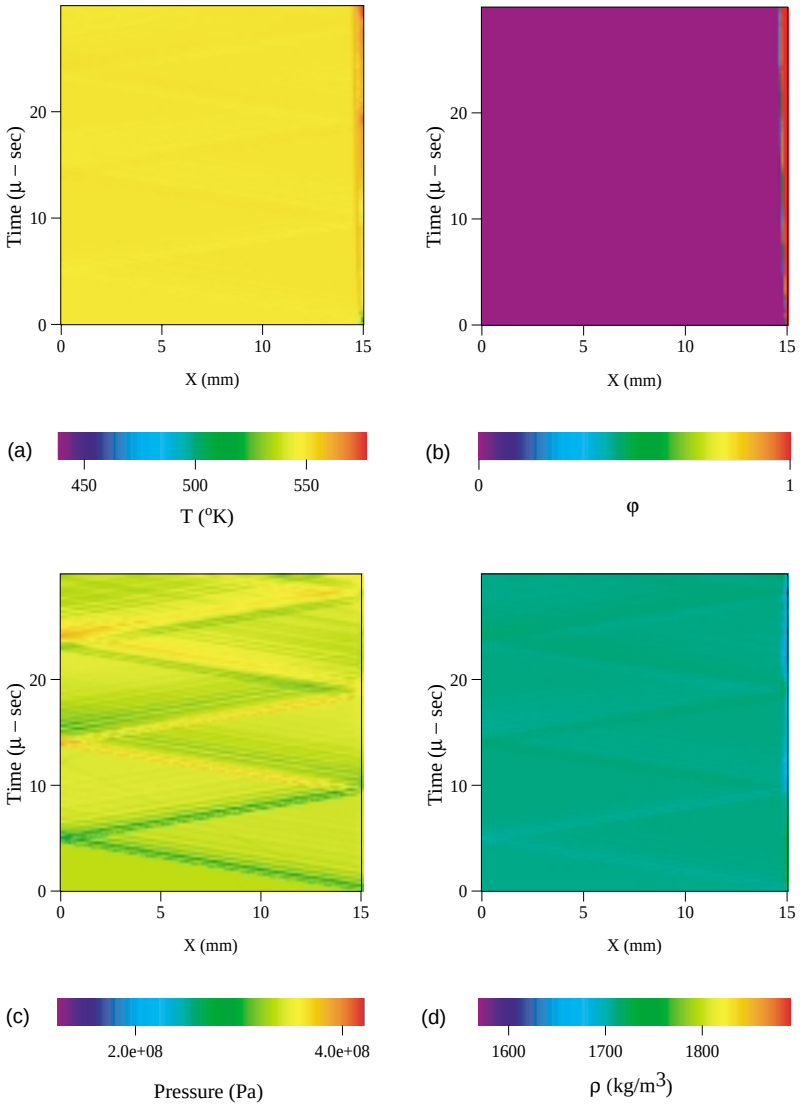

FIG. 10. *Temperature, phase, pressure, and density fields for a representative shear experiment* ($v_{shear} = 600\ m/s$, $T_0 = 550\ K$).

hybrid fashion to achieve high-order accuracy and stiffly stable calculation. A typical third-order method of this kind is given below:

$$\begin{aligned} \boldsymbol{k}_j &= a_j \boldsymbol{k}_{j-1} + h[\boldsymbol{f}(\boldsymbol{u}_{j-1}) + \boldsymbol{g}(\boldsymbol{u}_{j-1} + \bar{c}_j \boldsymbol{k}_{j-1} + c_j \boldsymbol{k}_j)], \\ \boldsymbol{u}_j &= \boldsymbol{u}_{j-1} + b_j \boldsymbol{k}_j \\ &\quad (j = 1, \ldots, 3), \end{aligned} \tag{5.1}$$

where h is the time increment, and the coefficients of the scheme are as follows:

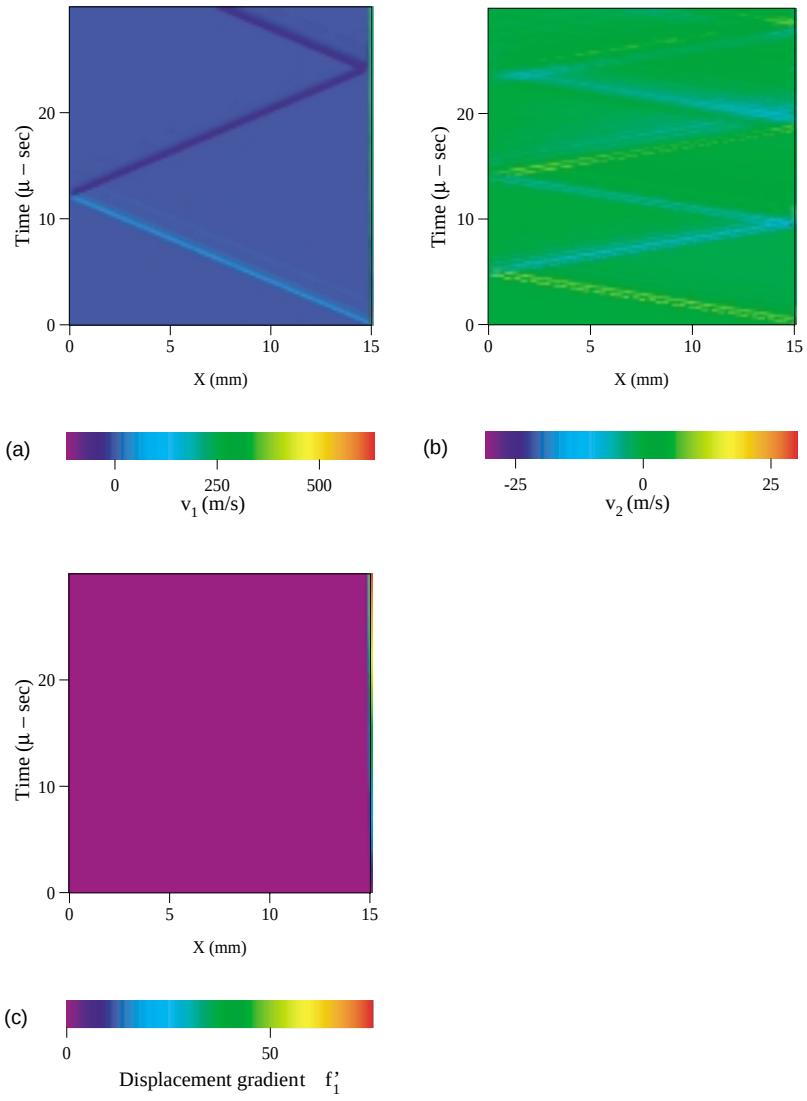

FIG. 11. *Shear velocity (v_1), compression velocity (v_2), and displacement gradient (du_1/dX_2) fields for a representative shear experiment ($v_{shear} = 600$ m/s, $T_0 = 550$ K).*

$$b_1 = \frac{1}{3}, \quad b_2 = \frac{15}{16}, \quad b_3 = \frac{8}{15}, \quad a_2 = -\frac{5}{9}, \quad a_3 = -\frac{153}{128},$$
$$c_1 = \frac{1}{5}, \quad c_2 = \frac{49}{75}, \quad c_3 = \frac{143}{600}, \quad \bar{c}_2 = -\frac{59}{135}, \quad \bar{c}_3 = -\frac{5283}{25600} \tag{5.2}$$

with $a_1 = 0, \bar{c}_1 = 0$.

In many instances where implicit calculation is not required, one can simply assign zero to the stiff vector $\boldsymbol{g}$ and assign the entire source as a nonstiff vector $\boldsymbol{f}$ and the standard explicit Runge–Kutta scheme is recovered.

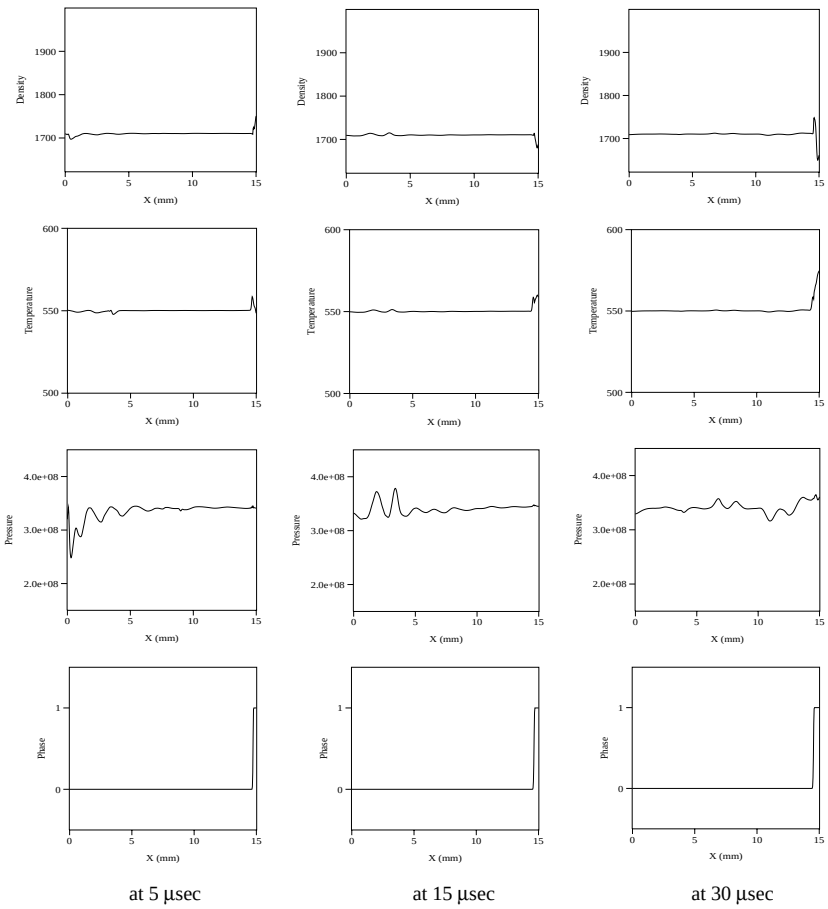

FIG. 12. *Snapshots of density, temperature, pressure, and phase field (from top to bottom) taken at time* $t = 5,\ 15,\ 30\,\mu$*sec from Figures* 10 *and* 11 *of the plane shearing experiment.*

5.2. Implementation. Before starting the computation one writes the governing PDEs in a conservative form such that limiting forms of the equations admit discontinuous solutions which are also admitted by the numerical approximation. Further, the stiff and nonstiff terms must be intelligently separated. In particular, convective terms, which are a priori discretized in space via a fourth-order convex ENO scheme, are always treated as nonstiff terms. The viscous stress terms of momentum equations are treated as nonstiff and are discretized by a fourth-order central differencing. Only the reaction source term, Ω, is treated as stiff and is subjected to the implicit numerical procedure. Otherwise the explicit method solves all the remaining terms of the equations.

We consider the shear motion to illustrate the numerical implementation. After converting the equations into a conservative form and separating the stiff and nonstiff terms, we can write the conservative variables and the fluxes as follows:

$$\text{(5.3)}\quad \boldsymbol{u} = \begin{bmatrix} \rho \\ \rho v_1 \\ \rho v_2 \\ \rho c_v T \\ \rho\phi \\ \rho f_1' \\ \rho\lambda \end{bmatrix}, \quad \boldsymbol{f} = \begin{bmatrix} -\frac{\partial}{\partial x_2}(\rho v_2) \\ -\frac{\partial}{\partial x_2}(\rho v_1 v_2 + \sigma_{12}) \\ -\frac{\partial}{\partial x_2}(\rho v_2 v_2 + \sigma_{22}) \\ -\frac{\partial}{\partial x_2}(\rho c_v T v_2) + \omega_1 \\ -\frac{\partial}{\partial x_2}(\rho\phi v_2) + \omega_2 \\ -\frac{\partial}{\partial x_2}(\rho f_1' v_2) + \rho_0 \frac{\partial v_1}{\partial x_2} \\ -\frac{\partial}{\partial x_2}(\rho\lambda v_2) \end{bmatrix}, \quad \text{and } \boldsymbol{g} = \begin{bmatrix} 0 \\ 0 \\ 0 \\ 0 \\ 0 \\ 0 \\ \rho\Omega \end{bmatrix},$$

where ω_1 and ω_2 are the right-hand-side source terms of T and ϕ. The convective terms are discretized by the fourth-order convex ENO scheme [6] and the resulting semidiscretized equations $\boldsymbol{u}_t = \boldsymbol{f} + \boldsymbol{g}$ are a system of autonomous ODEs in $\boldsymbol{u}$ and are integrated in time via the third-order Runge–Kutta method as discussed earlier.

6. Simulations of longitudinal and shear motions. We have validated the code written for the full model through a series of graduated tests. Since equations that correspond to classical elastodynamics and classical gas dynamics can be obtained simply by suppressing the appropriate terms, limiting versions of the code can be used to solve problems with exact solutions, like standard Riemann problems or small amplitude linear wave propagation. These tests are fully documented in Yoh's Ph.D. thesis [11]. Similar test cases can be found in Ruderman's thesis [12]. For example, Riemann problems have been computed for a special case of an ideal gas. In the special limiting case of small-displacement elasticity for shear motions, with the assumption of constant material properties, one can show that there are dilatation waves that travel at $\sqrt{(\lambda_s + 2\mu_s)/\rho_0}$ and shear waves that travel at $\sqrt{\mu_s/\rho_0}$, where $\lambda_s = 2\mu_s\nu_c/(1 - 2\nu_c)$.

6.1. One-dimensional shear motions. Here we discuss representative solutions to an initial boundary-value problem that represents numerical experiments for shear motion. The problem set up is as follows: A slab of material 15 mm thick in the x_2-direction is initially at an elevated temperature and suddenly subjected to a constant velocity shearing motion at the edge $x_2 = 15$ mm while the edge at $x_2 = 0$ is held fixed. The material is thermally insulated. For the purpose of these experiments, the gas phase is suppressed and does not appear, hence the transitions documented here occur only between solid and liquid. We show representative results for two different initial conditions. First, we consider the initial temperature at 550 K with the constant shear velocity of 600 m/s, dubbed shear case A. In the second case, the initial temperature is slightly above the melting transition temperature at 560 K with a lower shearing velocity of 200 m/s, dubbed shear case B. Shear case B exhibits more complex dynamics associated with multiple regions of phase change. Both cases show generic elastic wave interactions and reflections within solid-fluid regions. The computational domain has 500 points spread uniformly over 15 mm.

Figures 10 and 11 show x_2-t contour plots of the thermodynamic variables T, ϕ, p, ρ, the velocities v_1 and v_2, and the displacement gradient $f_1'(X_2)$. Initially the hot sample, just below the melting temperature at 550 K, is exposed to the wall shear at 600 m/s. The rapid shearing at $x_2 = 15$ mm produces sufficient heating to cause rapid melting in a thin layer near the moving boundary. This is easily observed in Figure 10(a) and 10(b) for the temperature T and phase variable ϕ, respectively. The shearing motion is then confined mostly to a thin shear layer as seen in Figure 11(a) for velocity v_1 (in the direction of the imposed motion at $x_2 = 15$ mm). Note that the shear wave in the solid associated with v_1 is clearly observed as a wave that initially

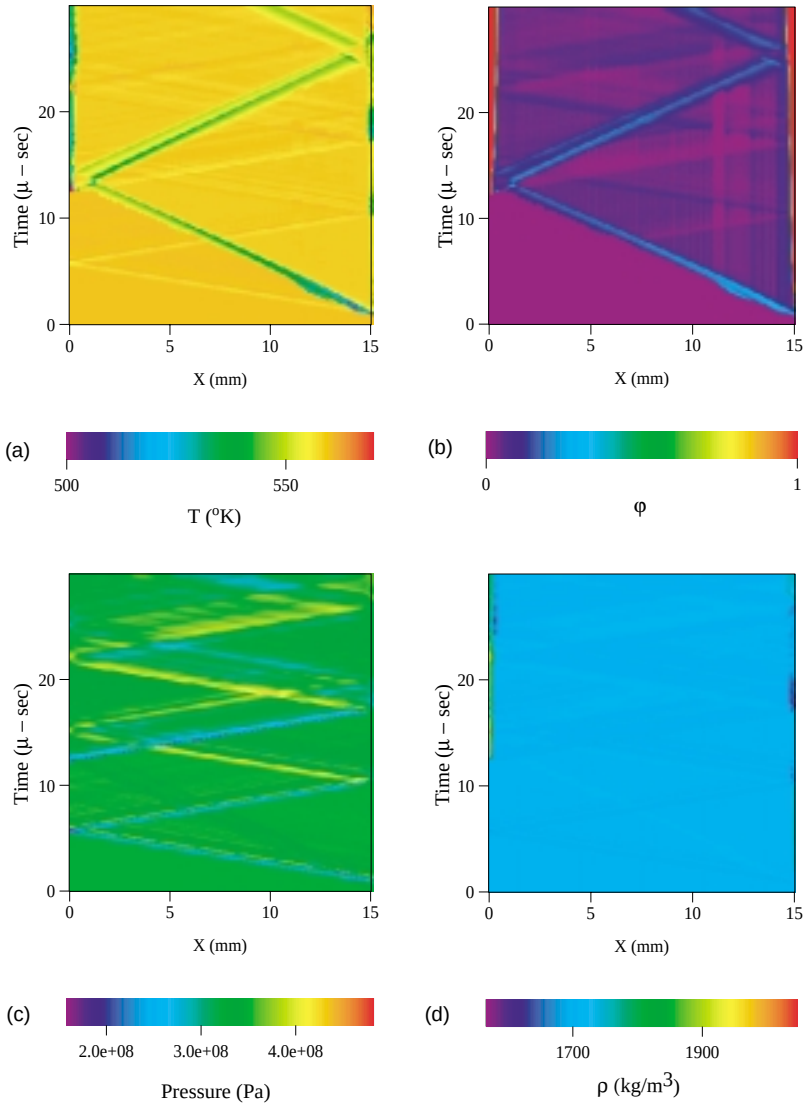

FIG. 13. *Temperature, phase, pressure, and density fields for a representative shear experiment* ($v_{shear} = 200$ *m/s*, $T_0 = 560$ *K*).

enters the domain at $x_2 = 15$ mm and travels toward $x_2 = 0$ mm and subsequently reflects off the stationary wall.

Figure 11(b) for v_2 displays waves that travel at the dilatational wave speed, which is approximately twice the shear wave speed. The dilatational waves are generated by the initial growth of the melted layer and are associated with pressure waves of magnitude of approximately 10^8 Pa = 1 kbar. Note that the initial stress in the system is elevated due to the effect of thermal expansion at the initially raised temperature. Close inspection of the temperature and pressure fields shown in Figure 10(a), (c) shows evidence of high frequency acoustic waves that can be traced to reflections and transmissions of waves through the solid/liquid interface near $x_2 = 15$ mm.

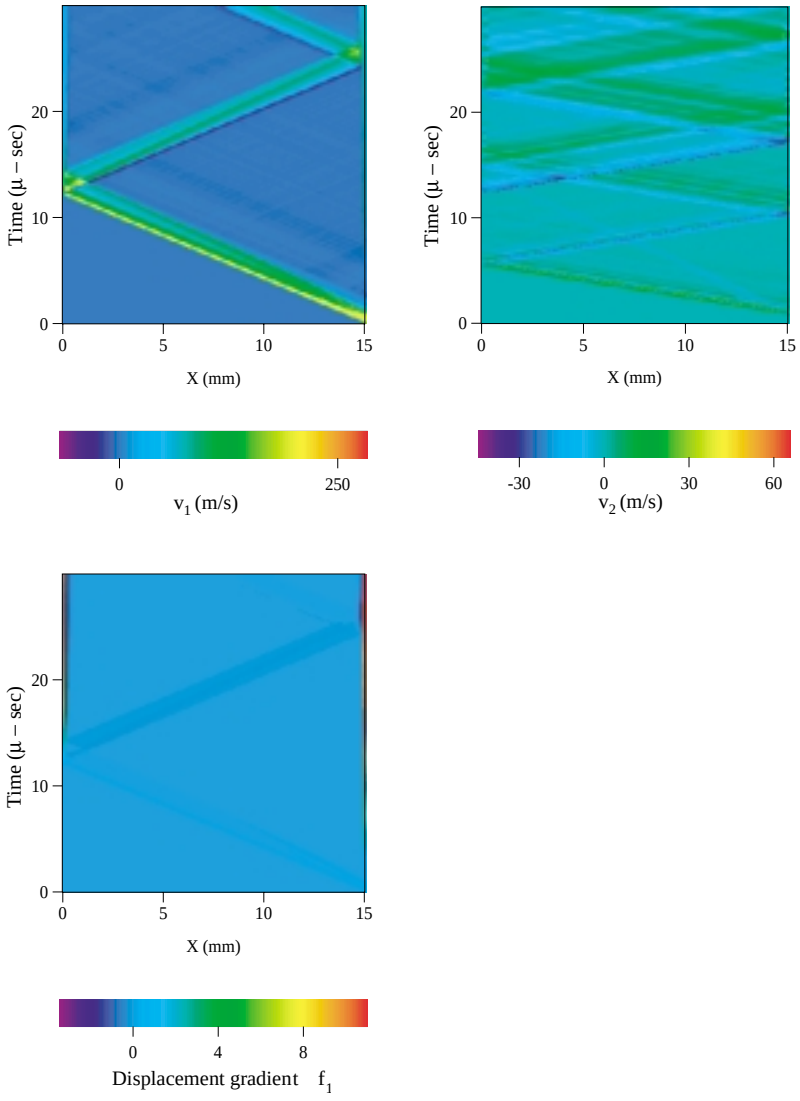

FIG. 14. *Shear velocity (v_1), compression velocity (v_2), and displacement gradient (du_1/dX_2) fields for a representative shear experiment ($v_{shear} = 200$ m/s, $T_0 = 560$ K).*

Figure 12 shows computed profiles for shear case A for ρ, T, p, and ϕ at times 5, 15, and 30 μsec, which represents time cuts across Figure 10(a)–(d). The profiles show elevated temperatures and phase change (melting) confined to the layer near the $x_2 = 15$ mm boundary. The fluctuations in the pressure, density, and temperature profiles are the result of the acoustic disturbances propagating through the solid and across the solid/liquid layer.

Note that the layer of liquid that develops at $x_2 = 15$ mm is a localized shear layer and can be thought of as a shear band. The material in the melt layer has very large v_1-velocities and subsequently undergoes large deformation. The material in the solid phase essentially remains fixed in place as the fluid layer slides across it.

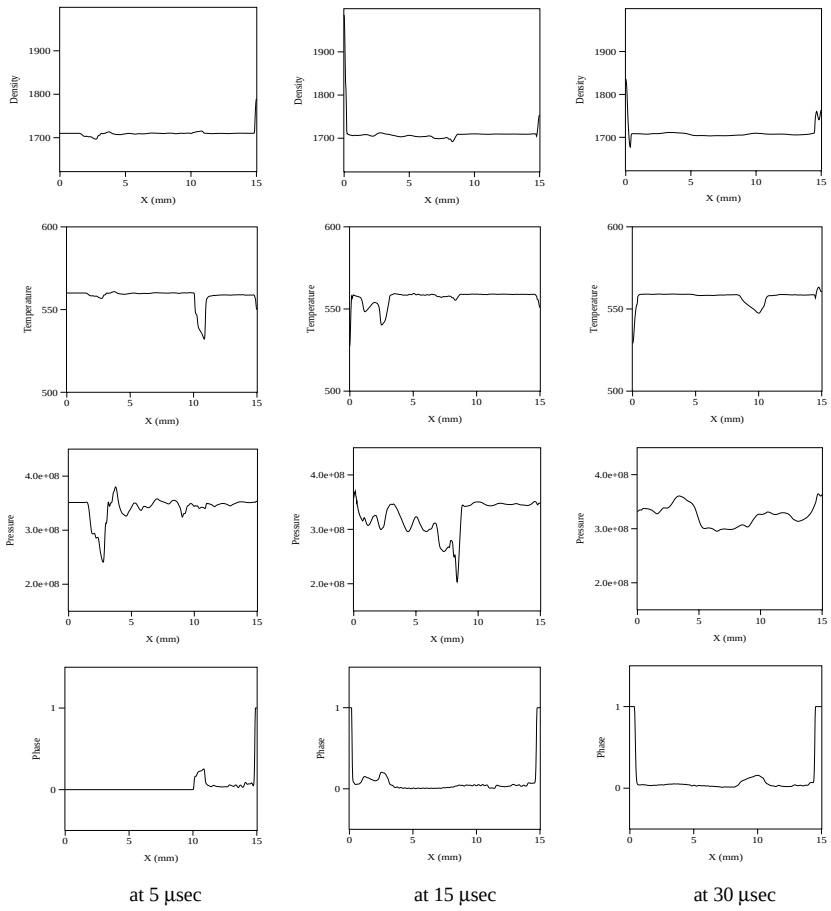

FIG. 15. *Instantaneous profiles of density, temperature, pressure, and phase field (from top to bottom) taken at time* $t = 5,\ 15,\ 30\,\mu$*sec corresponding to Figures* 13 *and* 14 *of the plane shearing experiment.*

Shear case B has the solid with its initial temperature slightly above the melt temperature, suddenly subjected to a (lower) constant shear motion of 200 m/s. As in case A, a melt layer forms near $x_2 = 15$ mm and the dilation wave travels across the slab. After reflection at the fixed wall, a second melt layer develops near $x_2 = 0$ mm. Figures 13, 14, and 15 show the additional complexity in the x_2-t record. The second melt layer causes additional scatter of waves generated near the $x_2 = 15$ mm boundary, and, in turn, the growth of the layer generates additional disturbances which transmit through the regions. One recalls that there are additional terms in the ϕ-evolution equation that are associated with the deformational part of the stress. We clearly see that the stress waves (by themselves) can induce the phase transformation. One sees transient phase generation carried on the subcharacteristics in the phase variable plot Figure 13(b). The next set of experiments for longitudinal motions illustrates shock melting.

6.2. One-dimensional longitudinal motion: Reverse impact. The results discussed next are for two different longitudinal motions where a HMX specimen of thickness 15 mm is initially solid at the melt temperature ($T = 558$ K) and subjected

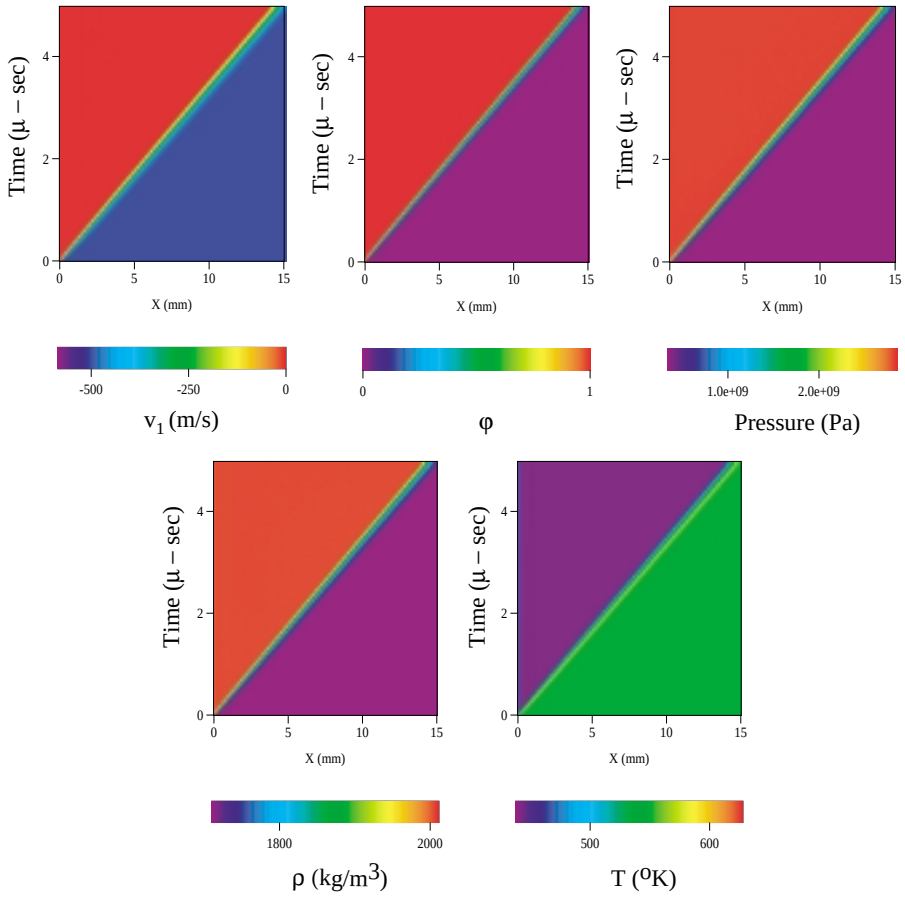

FIG. 16. *Velocity, phase, pressure, density and temperature fields for a representative reverse-impact (longitudinal) experiment ($v_{impact} = -500$ m/s, $T_0 = 550$ K).*

to a reverse impact at speed −500 m/s for longitudinal case A and −200 m/s for longitudinal case B. The computational domain spans the 0.015 m with 500 mesh points.

For longitudinal case A, Figures 16 and 17 illustrate the phenomenon of shock melting as predicted by the model. Figure 16(a)–(e) clearly shows the emergence of a shock wave from the stationary wall into the oncoming stream. Ahead of the shock the material is solid with $\phi = 0$; behind the shock the material is liquid with $\phi = 1$. The model predicts a shock with definite spatial structure as illustrated by the structure profiles taken at $t = 3\,\mu$sec and shown in Figure 17. In the shocked state, where the material has liquefied, there is a significant pressure increase to about 2.8 GPa (28 kbar)—a 20% density increase—and a drop in the temperature due to the endothermic nature of the phase transformation. The pressure and density rise monotonically across the shock structure. The temperature increases slightly, then drops with the onset of the phase transformation from solid to liquid. Throughout the structure, the phase changes monotonically from solid to liquid.

Longitudinal case B corresponds to a reverse-impact experiment where the impact speed is reduced to −200 m/s but the initial temperature is raised slightly to 560 K,

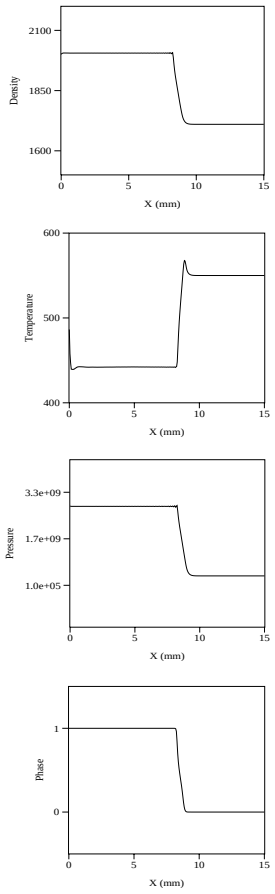

FIG. 17. *Snapshots of density, temperature, pressure, and phase field (from top to bottom) taken at time* $t = 3\,\mu$*sec from Figure* 16 *of the longitudinal exercise.*

just two degrees above the melt temperature. Figure 18 shows the x_1-t contour plots. Figure 19 shows corresponding line cuts taken at time $t = 3\,\mu$sec. Similar to longitudinal case A, shock induced phase transformation occurs; however, a stable intermediate phase is produced behind the shock front with $\phi = 0.33$. Interestingly, the model can be shown to allow these intermediate states in ϕ due to the contributions of the other stress-dependent source terms proportional to $\mu_s'(\phi), \mu_c'(\phi), \alpha_c'(\phi)$, etc. as found in (2.7). A complete analysis of all possible ϕ-states and their stability is beyond the scope of this paper. However, we can illustrate the stability of the intermediate state for longitudinal case B by a numerical evaluation as follows. We take the evolution equation for ϕ, (I 6.9), to be rewritten as $\frac{\partial \phi}{\partial t} = -v_1 \frac{\partial \phi}{\partial x_1} + w_2$, where w_2 is the source term for the material derivative of ϕ. We then take the shock structure as obtained numerically at $t = 3\,\mu$sec for both longitudinal cases A and B and plot $\partial\phi/\partial t$ versus ϕ in Figure 20. Stable equilibria points (in ϕ) are found by the zeros of $\partial\phi/\partial t$. For longitudinal case A, only $\phi = 0$ and $\phi = 1$ are stable with $\partial\phi/\partial t = 0$. But for longitudinal case B, the intermediate state $\phi = 0.33$ is found to be stable. Our numerical experiments suggest that increasing the intensity of the reverse impact causes the intermediate states to disappear with $\phi = 0, 1$ as the only

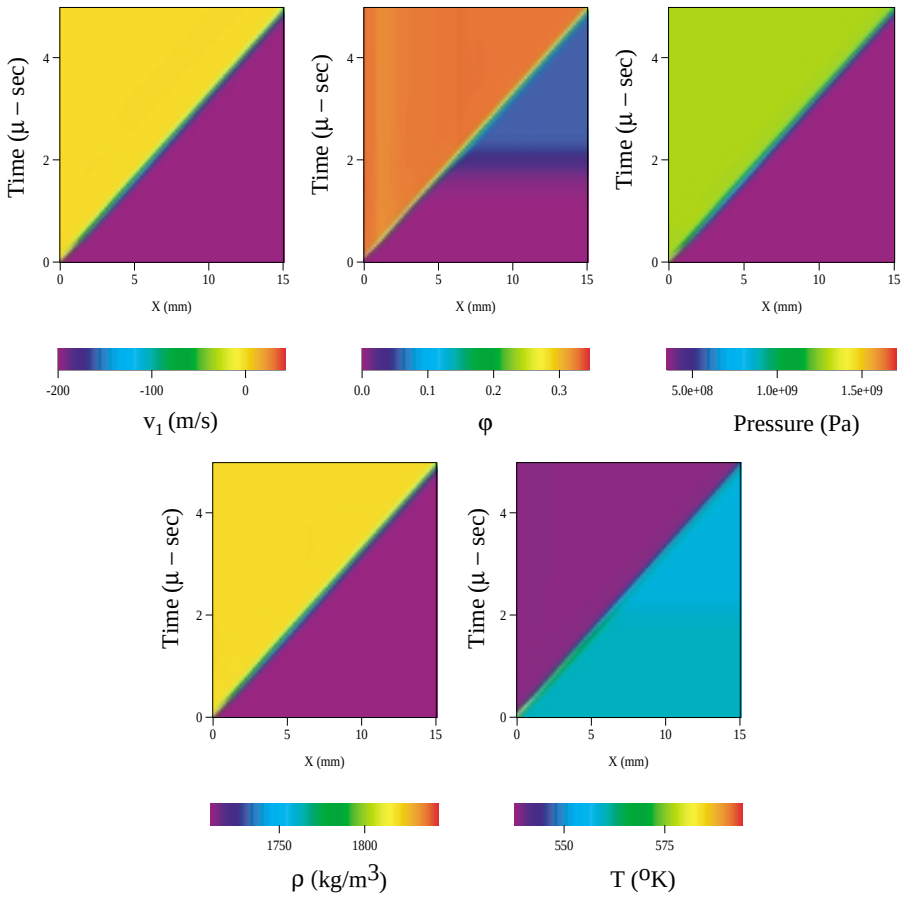

FIG. 18. *Velocity, phase, pressure, density and temperature fields for a representative reverse-impact (longitudinal) experiment ($v_{impact} = -200$ m/s, $T_0 = 560$ K).*

stable equilibria.

7. Conclusions. We have illustrated that our model, fitted to a real material, leads to predictions of simple motions (constant volume evolution, shear motion, and longitudinal motion) that are plausible. The model has the property that the constitutive theory automatically changes with the phase and is consistent with classical properties of that phase. We have shown that it is possible to fit the model to the known behavior of a real material.

Although idealized, the representative numerical experiments exhibit extremely rich behaviors. Strain localization phenomena occurred via melting in thin layers in many of the trials we have conducted. The phase change phenomena is directly coupled to the material loading through the change in material type and changes in properties that are carried with the phase. We are ready to apply this new continuum model to more complex physical problems of interest to us. Of course, extremely interesting and varied mathematical problems, such as steady traveling waves and their multidimensional stability, will arise that can profitably be analyzed by asymptotic means. The models embedded within this larger model may have greater application

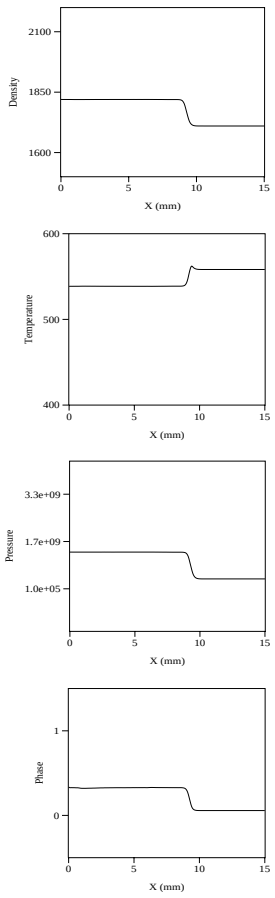

FIG. 19. *Snapshots of density, temperature, pressure, and phase field (from top to bottom) taken at time $t = 3\,\mu$sec from Figure* 18 *of the longitudinal experiment.*

to the general theory of phase transformation. Of specific near term interest to us is a detailed study of the mechanically induced ignition of an energetic solid. We also plan to pursue a simplified version of this model to more fully examine the processes of classical melting/freezing and vaporization/condensation in the context of the model. We also anticipate the near term application of the model to problems of vaporizing fuels and condensed phase propellant combustion.

Appendix. List of ϕ-dependent functions for $0 \le \phi \le 2$.

$$
\begin{aligned}
F(\phi) &= [\phi(\phi-1)(\phi-2)]^2 \\
F'(\phi) &= 2\phi(4 - 18\phi + 26\phi^2 - 15\phi^3 + 3\phi^4),
\end{aligned}
$$

$$
\begin{aligned}
\beta'_m(\phi) &= \begin{cases} 6\phi(1-\phi) & \text{for } 0 \le \phi \le 1, \\ 0 & \text{otherwise,} \end{cases} \\
\beta'_v(\phi) &= \begin{cases} 6(\phi-1)(2-\phi) & \text{for } 1 \le \phi \le 2, \\ 0 & \text{otherwise,} \end{cases}
\end{aligned}
$$

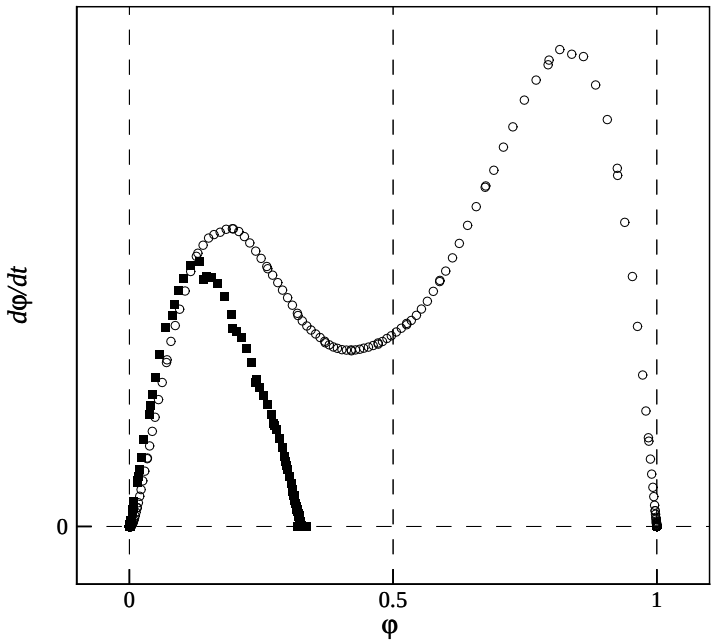

FIG. 20. *$d\phi/dt$ versus ϕ for the two specialized reverse-impact experiments discussed. By varying the initial temperature, T_0, meta-stable state ($\phi \approx 0.33$) is shown as a local equilibrium point on the experiment represented by the square symbols. In contrast, the experiment shown by hollow circles suggests that $\phi = 1$ is the only stable equilibria once the initial state is perturbed about the unstable point at $\phi = 0$, corresponding to the solid state under the impact loading.*

$$\mu_c(\phi) = \begin{cases} 2(\mu_{solid} - \mu_{liquid})\phi^3 - 3(\mu_{solid} - \mu_{liquid})\phi^2 + \mu_{solid} & \text{for } 0 \le \phi \le 1, \\ 2(\mu_{liquid})(\phi-1)^3 - 3(\mu_{liquid})(\phi-1)^2 + \mu_{liquid} & \text{for } 1 \le \phi \le 2, \end{cases}$$

$$\mu_c'(\phi) = \begin{cases} 6(\mu_{solid} - \mu_{liquid})\phi^2 - 6(\mu_{solid} - \mu_{liquid})\phi & \text{for } 0 \le \phi \le 1, \\ 6(\mu_{liquid})(\phi-1)^2 - 6(\mu_{liquid})(\phi-1) & \text{for } 1 \le \phi \le 2, \end{cases}$$

$$\mu_s(\phi) = \begin{cases} 2(\mu_{solid})\phi^3 - 3(\mu_{solid})\phi^2 + \mu_{solid} & \text{for } 0 \le \phi \le 1, \\ 0 & \text{for } \phi > 1, \end{cases}$$

$$\mu_s'(\phi) = \begin{cases} 6(\mu_{solid})\phi^2 - 6(\mu_{solid})\phi & \text{for } 0 \le \phi \le 1, \\ 0 & \text{otherwise,} \end{cases}$$

$$\mu_l(\phi) = \begin{cases} 2(-\mu_{liquid})\phi^3 - 3(-\mu_{liquid})\phi^2 & \text{for } 0 \le \phi \le 1, \\ 2(\mu_{liquid})(\phi-1)^3 - 3(\mu_{liquid})(\phi-1)^2 + \mu_{liquid} & \text{for } 1 \le \phi \le 2, \end{cases}$$

$$\mu_l'(\phi) = \begin{cases} 6(-\mu_{liquid})\phi^2 - 6(-\mu_{liquid})\phi & \text{for } 0 \le \phi \le 1, \\ 6(\mu_{liquid})(\phi-1)^2 - 6(\mu_{liquid})(\phi-1) & \text{for } 1 \le \phi \le 2, \end{cases}$$

$$R(\phi) = \begin{cases} 2(-R_{gas})(\phi-1)^3 - 3(-R_{gas})(\phi-1)^2 & \text{for } 1 \le \phi \le 2, \\ 0 & \text{for } \phi < 1, \end{cases}$$

$$R'(\phi) = \begin{cases} 6(-R_{gas})(\phi-1)^2 - 6(-R_{gas})(\phi-1) & \text{for } 1 \le \phi \le 2, \\ 0 & \text{otherwise,} \end{cases}$$

$$\alpha_c(\phi) = \begin{cases} 2(\alpha_{solid})(\phi-1)^3 - 3(\alpha_{solid})(\phi-1)^2 + \alpha_{solid} & \text{for } 1 \le \phi \le 2, \\ \alpha_{solid} & \text{for } \phi < 1, \end{cases}$$

$$\alpha_c'(\phi) = \begin{cases} 6(\alpha_{solid})(\phi-1)^2 - 6(\alpha_{solid})(\phi-1) & \text{for } 1 \le \phi \le 2, \\ 0 & \text{otherwise}, \end{cases}$$

$$\rho\gamma_\phi(\phi) = \begin{cases} 6(-\rho\gamma_\phi)\phi^2 - 6(-\rho\gamma_\phi)\phi & \text{for } 0 \le \phi \le 1, \\ 6(-\rho\gamma_\phi)(\phi-1)^2 - 6(-\rho\gamma_\phi)(\phi-1) & \text{for } 1 \le \phi \le 2, \end{cases}$$

$$c_v(\phi) = c_v$$

REFERENCES

[1] M. E. Gurtin, *Configurational Forces as Basic Concepts of Continuum Physics*, Appl. Math. Sci. 137, Springer-Verlag, New York, 2000.

[2] G. A. Ruderman, D. S. Stewart, and J. J.-I. Yoh, *A thermomechanical model for energetic materials with phase transformations*, SIAM J. Appl. Math., 63 (2002), pp. 510–537.

[3] T. B. Brill, *Multiphase chemistry considerations at the surface of burning nitramine monopropellants*, J. Propulsion Power, 11 (1995), pp. 740–750.

[4] J.-P. Poirier, *Introduction to the Physics of the Earth's Interior*, Cambridge University Press, Cambridge, UK, 1991.

[5] B. M. Dobratz and P. C. Crawford, *LLNL Explosive Handbook*, Lawrence Livermore National Laboratory, Livermore, CA, 1985.

[6] X.-D. Liu and S. Osher, *Convex ENO high order multi-dimensional schemes without field by field decomposition or staggered grids*, J. Comput. Phys., 142 (1998), pp. 304–330.

[7] R. Menikoff and T. D. Sewell, *Constituent properties of HMX needed for meso-scale simulations*, Appl. Phys. Rev., submitted.

[8] C. M. Tarver, S. K. Chidester, and A. L. Nichols, III, *Critical conditions for impact- and shock-induced hot spots in solid explosives*, J. Phys. Chem., 100 (1996), pp. 5794–5799.

[9] J. J. Yoh and X. Zhong, *Low-storage semi-implicit Runge–Kutta schemes for chemically reacting flow computations*, J. Comput. Phys., submitted.

[10] C. Yoo and H. Cynn, *Equation of state, phase transition, decomposition of β-hmx (octahydro-1,3,5,7-tetranitro-1,3,5,7-tetrazoncine) at high pressures*, J. Chem. Phys., 111 (1999), pp. 10229–10235.

[11] J. J. Yoh, *Thermomechanical and Numerical Modeling of Energetic Materials and Multimaterial Impact*, Ph.D. thesis, University of Illinois, Urbana-Champaign, IL, 2001.

[12] G. A. Ruderman, *A Continuum Thermomechanical Model for Energetic Materials*, Ph.D. thesis, University of Illinois, Urbana-Champaign, IL, 1998.

[13] D. Bedrov, G. D. Smith, and T. D. Sewell, *Temperature dependent shear viscosity coefficients of HMX, a molecular dynamics simulation study*, J. Chem. Phys., 112 (2000), pp. 7203–7208.